

PAPER • OPEN ACCESS

Divertor power load investigations with deuterium and tritium in type-I ELMy H-mode plasmas in JET with the ITER-like wall



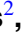







To cite this article: M. Faitsch *et al* 2023 *Nucl. Fusion* **63** 112013

View the [article online](#) for updates and enhancements.

You may also like

- [Characterizations of power loads on divertor targets for type-I, compound and small ELMs in the EAST superconducting tokamak](#)
L. Wang, G.S. Xu, H.Y. Guo et al.
- [Investigation of scrape-off layer and divertor heat transport in ASDEX Upgrade L-mode](#)
B Sieglin, T Eich, M Faitsch et al.
- [Scaling of divertor power footprint width in RF-heated type-III ELMy H-mode on the EAST superconducting tokamak](#)
L. Wang, H.Y. Guo, G.S. Xu et al.

Divertor power load investigations with deuterium and tritium in type-I ELMy H-mode plasmas in JET with the ITER-like wall

M. Faitsch^{1,*} , I. Balboa² , P. Lomas² , S.A. Silburn² , A. Tookey² , D. Kos² ,
A. Huber³ , E. de la Luna⁴ , D. Keeling² , A. Kappatou¹  and JET Contributors^a

¹ Max-Planck-Institute for Plasma Physics, Boltzmannstr. 2, D-85748 Garching, Germany

² United Kingdom Atomic Energy Authority, Culham Science Centre, Abingdon, Oxon OX14 3DB, United Kingdom of Great Britain and Northern Ireland

³ Forschungszentrum Jülich GmbH, Institut für Energie- und Klimaforschung, Plasmaphysik, 52425 Jülich, Germany

⁴ Laboratorio Nacional de Fusión, CIEMAT, Madrid, Spain

E-mail: Michael.Faitsch@ipp.mpg.de

Received 1 March 2023, revised 26 May 2023

Accepted for publication 13 June 2023

Published 12 October 2023



CrossMark

Abstract

Divertor power load is a major challenge towards a burning plasma in a next-step tokamak. Here, the first results of a divertor power load characterisation in tritium plasmas in type-I ELMy H-mode, obtained in the JET deuterium-tritium campaign (DTE2) performed in 2021, are presented. It is demonstrated that both, transient loads due to type-I ELMs as well as the power fall-off length, do not exhibit an explicit ion mass dependence, with remarkably similar values in the tritium plasmas and in the deuterium references. This gives an improved credence to published scaling law predictions, solely based on deuterium plasma experiments. Moreover, the type-I ELM impact on the inner divertor target is studied in deuterium discharges. A slightly increased parallel energy fluence on the inner target with a factor of 1.08 compared to the outer target is observed. This is explained by the smaller major radius of the inner target.

Keywords: tritium, power exhaust, type-I ELMs, power fall-off length, tokamak, JET, divertor

(Some figures may appear in colour only in the online journal)

^a See the author list of “Overview of T and D-T results in JET with ITER-like wall” by C.F. Maggi *et al* to be published in *Nuclear Fusion Special Issue: Overview and Summary Papers from the 29th Fusion Energy Conference (London, UK, 16–21 October 2023)*.
* Author to whom any correspondence should be addressed.



Original Content from this work may be used under the terms of the [Creative Commons Attribution 4.0 licence](https://creativecommons.org/licenses/by/4.0/). Any further distribution of this work must maintain attribution to the author(s) and the title of the work, journal citation and DOI.

1. Introduction

Two main challenges for power exhaust in H-mode operation are the transient loads due to type-I edge localised modes (ELMs) and the steady state power load. The latter is tightly linked to the width of the power carrying layer in the scrape-off layer, the power fall-off length λ_q . Unmitigated divertor power loads in next step fusion devices like ITER are extrapolated to be close to or to exceed material limits [1, 2] making significant impurity seeding necessary. The amount of required injected impurities depends strongly on the scrape-off layer width [3, 4].

A multi-machine data set for deuterium H-mode plasmas in JET, DIII-D, ASDEX Upgrade, C-Mod, NSTX and MAST found that the poloidal magnetic field strength is the main parameter determining λ_q [5]. This is confirmed by a heuristic drift-based model (HDM), finding the poloidal gyro-radius as main scaling parameter [6].

In addition, a variety of experimental studies in recent years focused on correlating confinement properties with λ_q . These studies report that higher confinement correlates with a more narrow λ_q , independent of the confinement regime, reported for Alcator C-Mod [7] and ASDEX Upgrade [8], with the exceptions of the quasi-continuous exhaust regime [9]. This trend was also observed in type-I ELMy H-mode in JET with both carbon (JET-C) and ITER-like wall (JET-ILW) [10].

The vast majority of λ_q studies are performed in deuterium plasmas. Reported experimental investigations with varying main ion species do not provide a uniform picture and are mostly conducted in L-mode plasmas. A study comparing JET and ASDEX Upgrade L-mode measurements in deuterium and hydrogen reports on no significant changes in λ_q with isotope species [11]. A newer study in ASDEX Upgrade in L-mode found that λ_q in hydrogen is broader compared to deuterium, attributing the change to the lower pedestal temperature in hydrogen discharges [12]. Helium and deuterium discharges in TCV did not exhibit a considerable difference in L-mode [13]. A study on the inter-ELM wetted area in JET with hydrogen, deuterium and helium indicated no effect of the mass and a weak dependence on the charge of the main ions [14].

The divertor impact of type-I ELMs is characterised by the so called energy fluence, the spatial peak value of the time integrated power load for the duration of the ELMs. The type-I ELM energy fluence increases with increasing pedestal top pressure and machine size both experimentally and in a model based on energy balance considerations [15]. This model does not predict an explicit ion mass dependence. Recent works report on a material limit of $0.15\text{--}0.5 \frac{\text{MJ}}{\text{m}^2}$ [16–18] for transients with a duration of $\tau_{\text{ELM}} = 500 \mu\text{s}$ (full width at half maximum) for ITER [16]. Similar to inter-ELM studies, also for type-I ELMs mainly deuterium discharges are studied. Main ion species studies of the ELM wetted area in JET with hydrogen, deuterium and helium discharges revealed neither a mass nor charge dependence [14]. Similarly, a study of the integrated power to the outer divertor target at similar ELM loss fraction in helium and deuterium in ASDEX Upgrade presents no significant differences between the species [19].

Furthermore, most type-I ELM studies are conducted on the outer divertor target. This is because of the higher steady state power fraction reaching the outer divertor target compared to the inner. However, understanding the asymmetry between the inner and outer target is important because the maximum tolerable ELM size depends on the material limit of both divertor targets. In this contribution, a specifically infrared thermography (IR) optimised shape in JET is exploited to obtain simultaneous measurements on both the inner and outer divertor. The reported ratio between inner and outer parallel energy fluence is about unity for ASDEX Upgrade [15] and DIII-D [20].

In this work, the first results of a divertor power load characterisation in type-I ELMy H-mode tritium plasmas are presented. They are obtained in the JET deuterium-tritium campaign (DTE2) performed in 2021 with the ITER-like wall and represent a unique opportunity to improve the credence to published scaling law predictions, solely based on deuterium (D) plasma experiments. In particular, the tritium (T) data allows us to check for an isotope mass dependence compared to a gyro-radius scaling of the power fall-off length. It especially strengthens the extrapolation towards a burning plasma in ITER and other future tokamaks that will use a mixture of deuterium and tritium as fuel.

The two key experimental objectives of the presented study are (i) the explicit impact of the isotope mass on λ_q and type-I ELM energy fluence and (ii) type-I ELM energy fluence measurements on both inner and outer target. Included in the original plan within the first objective was to extend the poloidal magnetic field strength range towards larger values ($I_p > 3.5 \text{ MA}$, $B_{\text{pol,MP}} > 0.7 \text{ T}$). This is because modelling using the XGC1 code demonstrate a deviation from the multi-machine scaling law of the power fall-off length at large major radius and high poloidal magnetic field [21]. This is caused by a change of the nature of the underlying turbulence leading to a bifurcation with respect to the poloidal magnetic field and leads to an increased power fall-off length extrapolation for ITER [21]. However, due to machine limitations and the prioritisation for developing the D-T target plasmas, the envisaged high poloidal magnetic field was not achieved.

This article is organised as follows: section 2 introduces the data base of deuterium and tritium discharges used for the presented study. The results for the type-I ELM energy fluence are presented in section 3. Section 4 highlights the similarity of the power fall-off length in deuterium and tritium. A summary and conclusions are presented in section 5.

2. Database overview

A set of IR optimised plasma pulses was executed between 2016 and 2022. The main focus of these pulses is the simultaneous measurement of both inner and outer strike line location in steady state type-I ELMy H-mode phases. In order to achieve this goal, an optimised shape was developed in 2016. Figure 1 shows the lower part of the poloidal cross-section of JPN 100 181 highlighting the separatrix and field lines in the scrape-off layer. Both, inner and outer strike lines

Table 1. Main parameters of the analysed data sets. ELM frequency f_{ELM} , strength of the toroidal magnetic field on axis B_{tor} , plasma current I_p , edge safety factor q_{95} , heating power P_{heat} , normalised pressure β_N as well as pedestal top density $n_{e,\text{ped}}$, temperature $T_{e,\text{ped}}$ and pressure $p_{e,\text{ped}}$.

| Name | ELMs | | | λ_q | |
|---|---------|---------|---------|-------------|---------|
| | D outer | D inner | T outer | D outer | T outer |
| # points | 25 | 14 | 9 | 30 | 9 |
| # pulses | 19 | 9 | 4 | 22 | 4 |
| f_{ELM} (Hz) | 19–94 | 14–76 | 32–79 | 19–94 | 32–79 |
| $ B_{\text{tor}} $ (T) | 1.3–3.1 | 1.2–2.7 | 1.7–2.4 | 1.5–3.1 | 1.7–2.4 |
| I_p (MA) | 1.4–2.7 | 1.4–2.4 | 1.7–2.1 | 1.5–2.7 | 1.7–2.1 |
| q_{95} | 2.6–3.9 | 2.6–3.9 | 3.2–3.7 | 2.6–3.9 | 3.2–3.7 |
| P_{heat} (MW) | 10–27 | 12–20 | 10–17 | 10–27 | 10–17 |
| β_N | 1.7–3.3 | 1.7–3.3 | 1.6–2.6 | 1.7–3.3 | 1.6–2.6 |
| $n_{e,\text{ped}}$ (10^{19} m^{-3}) | 3.0–6.5 | 3.0–6.5 | 4.1–5.0 | 3.0–6.5 | 4.1–5.0 |
| $T_{e,\text{ped}}$ (keV) | 0.5–1.2 | 0.5–0.9 | 0.7–1.1 | 0.5–1.2 | 0.7–1.1 |
| $p_{e,\text{ped}}$ (kPa) | 3.2–7.9 | 3.2–7.9 | 4.8–8.0 | 3.4–7.9 | 4.8–8.0 |

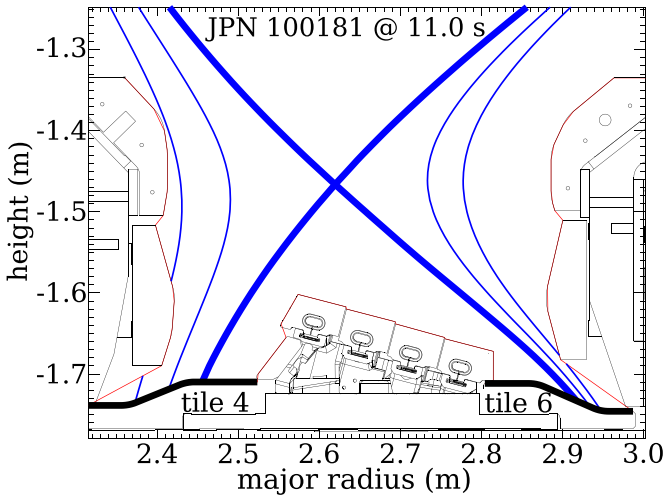


Figure 1. Divertor configuration for an IR optimised shape. Shown are the separatrix and scrape-off layer field lines for JPN 100 181 at 51.0 s.

intersect the horizontal divertor tiles, called tile 4 and tile 6, respectively. Operating with the outer strike line on tile 6 exhibits improved H-mode core and pedestal performance in JET-ILW compared to other strike line locations [22]. This specific configuration allows a maximised amount of scrape-off layer field lines to intersect tile 6, important for measuring the scrape-off layer quantities at the outer horizontal divertor target plate. The main diagnostics at the divertor targets are the IR thermography systems. The details of the IR analysis routine is explained in the [appendix](#).

The same configuration is used for measurements in tritium plasmas. However, the camera observing the inner target was not available for the here reported experiments in tritium because it had to be removed for the D-T campaign. As it will be discussed in the following sections, the main parameters influencing the type-I ELM and inter-ELM properties are the pedestal top density and pressure as well as the toroidal and poloidal magnetic fields.

The primarily changed parameters in this data set are the plasma current and toroidal magnetic field strength. Plasma fuelling and heating are adjusted in order to achieve stationary conditions in density, ELM behaviour and radiation at heating power levels clearly above the transition power to H-mode, thus, maintaining a regular ELM frequency typically above 30 Hz. Both the elongation of $\kappa = 1.7$ and the averaged triangularity of $\delta = 0.29$ are kept constant. The main plasma parameters for the various data sets are summarised in table 1. We deduce that the ELMs presented in this article can be considered type-I ELMs due to the similarity in the engineering parameters and ELM frequency as the ones reported in a comprehensive pedestal study of a JET-ILW database by Frassinetti *et al* [23].

The pedestal top pressure is the main scaling parameter for the type-I ELM energy fluence, while the poloidal magnetic field strength is the main scaling parameter for the power fall-off length. An increase in plasma current (poloidal magnetic field strength) leads to an about linear increase in pedestal top pressure in our data set. This is a consequence of the way the data set is constructed, with increased heating power at higher plasma current and toroidal magnetic field strength to ensure stationary conditions.

The electron kinetic profiles are obtained with the high resolution Thomson scattering (HRTS, [24]) system. An ELM filtering is applied, using only data points in the second half (0.5–0.95) of the ELM cycle. This enlarged range compared to typical studies using the last 30%, e.g. [23], in some cases is needed to get HRTS profiles within the considered time window. Using only data points between 0.75 and 0.95 leads to the same result for the time windows that also have HRTS profiles in the more narrow range. The pedestal top data is extracted by fitting a modified hyperbolic tangent (mtanh, [25]) function onto the profiles and taking the values corresponding to one width inside the symmetry point.

Figure 2 displays the pedestal composition as well as the about linear increase of pedestal pressure with plasma current. It is observed that the increase in plasma current mainly increases the pedestal top density, consistent with previous

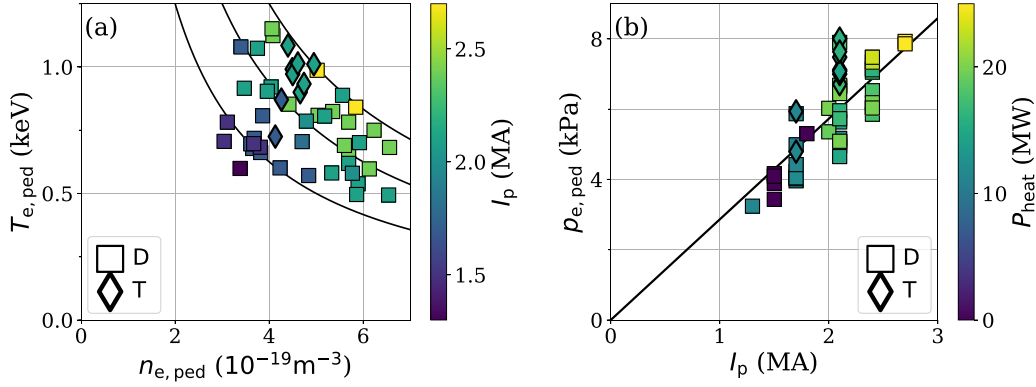


Figure 2. Pedestal top kinetic values for the deuterium (squares) and tritium (diamonds) data set. (a) Pedestal top temperature $T_{e,ped}$ versus pedestal top density $n_{e,ped}$. The black lines are lines of constant pressure ([4, 6, 8] kPa). The plasma current I_p is color-coded. (b) Pedestal top pressure $p_{e,ped}$ versus plasma current I_p . The line represents a linear regression with slope $2.9 \frac{\text{kPa}}{\text{MA}}$. The heating power P_{heat} is color-coded.

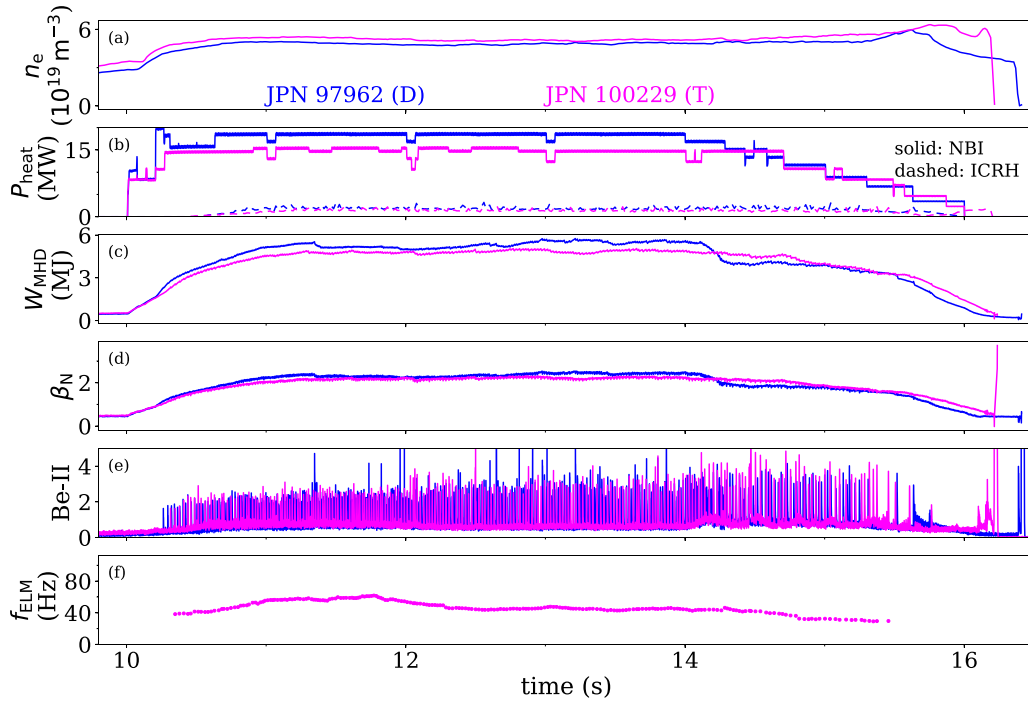


Figure 3. Time traces of a deuterium (blue) and tritium (magenta) pair of plasmas. They have the same toroidal magnetic field, plasma current and shaping. The graphs show (a) the core line averaged density, (b) the heating power from ICRF (dashed lines) and NBI (solid lines), (c) stored energy W_{MHD} , (d) normalised plasma pressure β_N , (e) the Be-II line emission as ELM monitor and (f) the ELM frequency.

studies [23]. The strong link between poloidal magnetic field and pedestal top pressure and density does not pose a significant bias in the following analysis. However, due to the strong link between them, both poloidal magnetic field and pedestal top density will be separately discussed as scaling parameter for the power fall-off length. The plasmas in tritium discussed here are based on deuterium reference pulses and are stable pulses with an ELM frequency of around 50 Hz, similar to the deuterium pulses. For this, heating power and/or gas fuelling levels are adjusted. The tritium plasmas have a very similar qualitative behaviour as the deuterium reference pulses.

The pedestal pressure for the T plasmas is slightly higher than the D plasmas for the same I_p . Since the experiment was

not done at constant engineering parameters, no conclusion on how the isotope mass affects the pedestal can be extracted. For a detailed analysis of the isotope mass impact on the pedestal see [26, 27]. It is therefore noted that no detailed comparison between individual pulses is performed here, the analysis for the ELM energy fluence and power fall-off length is done in a data base approach.

A comparison between a deuterium reference pulse and the tritium counter-part is presented in figure 3. The tritium plasma pulse has a slightly lower NBI input power, leading to a similar stored energy and normalised pressure. The ELM frequency is slightly lower in the tritium plasma.

The resulting pedestal profiles of electron density and temperature in the tritium plasmas are very similar to the profiles

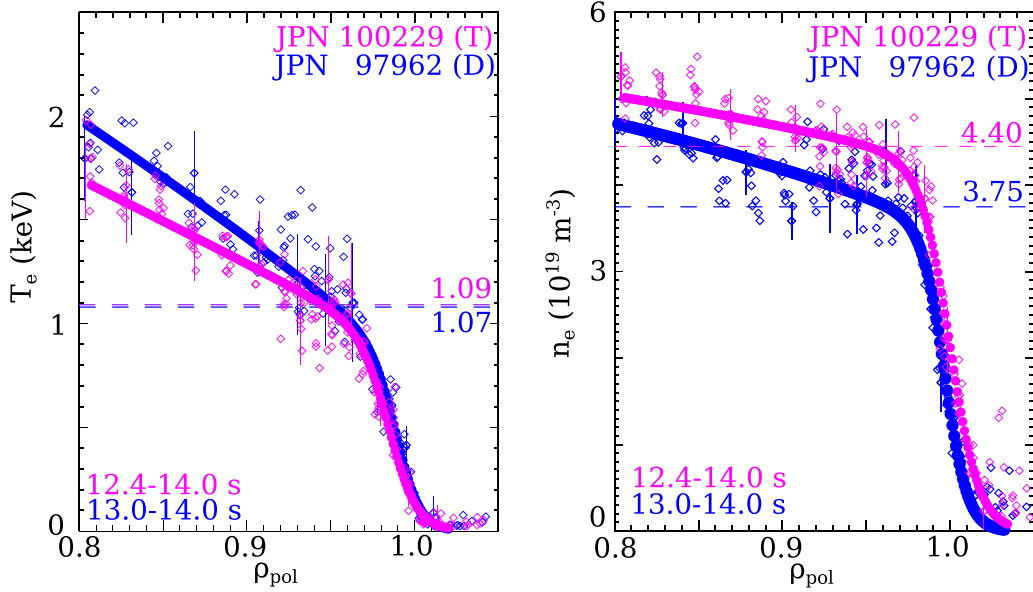


Figure 4. Electron pedestal kinetic profiles from the HRTS system for a deuterium (blue) and tritium (magenta) pair of plasmas. The lines represent the mtanh fit onto the data points.

in the deuterium plasmas. The pedestal profiles for the same pair of tritium and deuterium plasmas are presented in figure 4. The pedestal top pressure is slightly higher in tritium due to a higher density. The general trend of higher pedestal top density in tritium plasmas is consistent with the behaviour observed throughout the tritium campaign [26, 27].

Only steady state type-I ELMy H-mode phases, with constant heating and fuelling, have been included in the analysis presented here. Most pulses have two levels of fuelling, leading to multiple steady state time windows for the analysis. The length of the time windows varies between 0.3 s and 3.2 s.

3. Type-I ELM divertor impact

The main parameter for the divertor impact of transients is the peak energy fluence

$$\epsilon_{\text{div}} = \max_s \int_{t_{\text{ELM}}} q(s, t) dt \quad (1)$$

with the divertor heat flux q along the divertor coordinate s and time t . The integration in time is performed for the duration of the transient t_{ELM} . In order to compare different experiments, the energy fluence is mapped parallel to the magnetic field

$$\epsilon = \frac{\epsilon_{\text{div}}}{\sin(\alpha_{\text{div}})} \quad (2)$$

with the angle between the divertor target and the magnetic field lines α_{div} in the order of 4° for the presented data set, calculated for each time window separately.

Energy balance considerations lead to a model by Eich *et al* [15]:

$$\epsilon_{\text{model,fix}} \left(\frac{\text{MJ}}{\text{m}^2} \right) = 6 \cdot 10^{-6} \cdot \pi \cdot a(\text{m}) \cdot \hat{\kappa} \cdot p_{\text{e,ped}}(\text{Pa}) \cdot \frac{B_{\text{tor,MP}}(\text{T})}{B_{\text{pol,MP}}(\text{T})} \quad (3)$$

with a minor radius, $\hat{\kappa} = \sqrt{\frac{1+\kappa^2}{2}}$ effective elongation, $p_{\text{e,ped}}$ pedestal top electron pressure and $B_{\text{tor,MP}}$, $B_{\text{pol,MP}}$ toroidal and poloidal magnetic field at the outer mid-plane (MP), respectively.

In the following, we relax one simplification (the model as presented in equation (3) assumes that the major radius of the divertor target and of the geometrical axis are equal, $R_{\text{div}} = R_{\text{geo}}$) due to the varying major radii of the inner and outer divertor leading to

$$\epsilon_{\text{model}} = \epsilon_{\text{model,fix}} \cdot \frac{R_{\text{geo}}(\text{m})}{R_{\text{div}}(\text{m})}. \quad (4)$$

This model does not have an explicit isotope dependence. However, it assumes similar ion and electron pressure at the pedestal top.

It is important to note that the experimental data used to develop the model falls within a range of unity and three times the scaling prediction [28]. This natural scatter of three is not explained so far. Experiments at DIII-D found that larger energy fluence is observed close to the H-mode threshold power [20].

3.1. Impact on inner vs outer divertor in deuterium plasmas

As a first step, we present the outer target energy fluence measurements in figure 5. The measurements fall well within the model prediction (between the 1:1 and 3:1 lines) and reported data from previous JET experiments [15]. The markers represent the median (50th percentile) within a steady state time

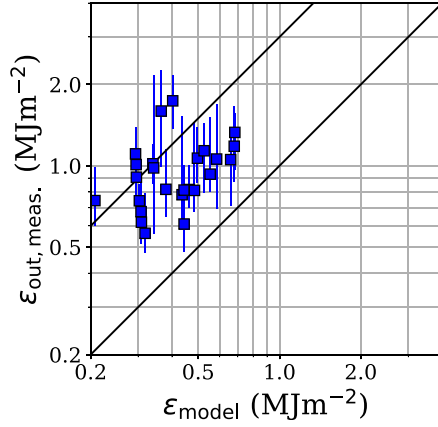


Figure 5. Type-I ELM energy fluence measured on the outer divertor target $\epsilon_{\text{out, meas.}}$ in deuterium plasma pulses compared to the model prediction ϵ_{model} in a log-log plot. The 1:1 and 3:1 lines are shown in black.

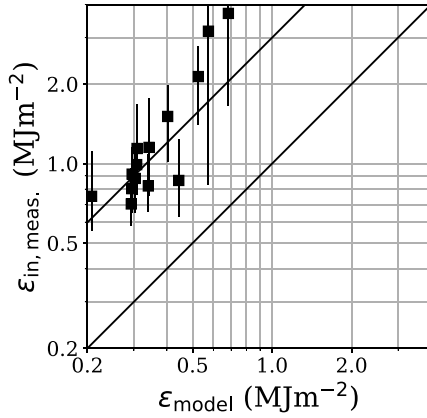


Figure 6. Type-I ELM energy fluence measured on the inner divertor target $\epsilon_{\text{in, meas.}}$ in deuterium plasma pulses compared to the model prediction ϵ_{model} in a log-log plot. The 1:1 and 3:1 lines are shown in black.

window while the error-bars represent the 33rd and 66th percentiles.

As a second step, we present the inner target energy fluence measurements in figure 6. These are the first reported energy fluence data for the inner target in JET. It is demonstrated that also the inner target data fall within the model prediction (between the 1:1 and 3:1 lines), although they are clearly on the upper end of the prediction.

As a next step, the measurements on both targets are compared to each other. The asymmetry between inner and outer target measurements is highlighted in figure 7. The ratio between inner and outer data is $\frac{\epsilon_{\text{in}}}{\epsilon_{\text{out}}} = 1.08$. This is very close to the model prediction of $\frac{\epsilon_{\text{model, in}}}{\epsilon_{\text{model, out}}} = \frac{R_{\text{div, out}}}{R_{\text{div, in}}} = 1.16$. A ratio close to unity is also reported for ASDEX Upgrade [15] and DIII-D [20].

Two effects are present when comparing the divertor impact of ELMs on the inner and outer target. On the one hand, as presented in this experimental study as well as in the model by Eich *et al*, the smaller major radius of the inner target

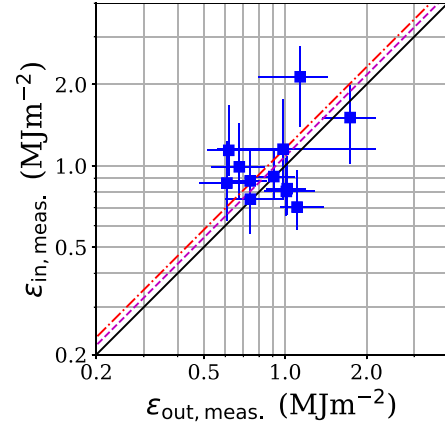


Figure 7. Type-I ELM energy fluence comparison between inner $\epsilon_{\text{in, meas.}}$ and outer target $\epsilon_{\text{out, meas.}}$ in a log-log plot. The black line represents unity. The dashed red line has a slope of 1.16 and represents the prediction from the model due to the major radius difference between the two targets. The dashed magenta line is a linear regression with a slope of 1.08.

leads to a slightly larger parallel energy fluence. On the other hand, the toroidal magnetic field at the inner target is larger, leading to a smaller field line incidence angle and, hence, to a reduced projection of the parallel energy fluence onto the divertor ϵ_{div} . In fact, the two effects, smaller major radius and higher toroidal magnetic field, cancel each other nearly perfectly. This is, because the toroidal field decreases with $1/R_{\text{div}}$ and the parallel energy fluence decreases with R_{div} , thus, the target impact following the model prediction is independent on major radius.

However, this is only true for a perfectly aligned toroidal divertor structure. Any misalignments on the inner target are more severe due to the smaller field line incidence angle. Furthermore, tile gap loading is more challenging on the inner target [29–31].

As a conclusion, the data presented here for the inner target is very valuable for modelling and extrapolation towards next step devices like ITER, where the inner target is likely more challenging for transient power loads due to the above mentioned reasons. The similarity of the measured energy fluence on the inner target to the outer target data, together with the match to the prediction of the model by Eich *et al*, strengthens the applicability of the extrapolation.

3.2. Comparison between pulses in deuterium and tritium

A novelty of the presented data sets are measurements in tritium plasmas. A comparison between energy fluence measurements on the outer target in deuterium and tritium plasmas is presented in figure 8. The measured values for both deuterium and tritium plasmas follow the model prediction within the two boundaries. The data points from the tritium plasmas have a slightly increased pedestal top pressure compared to the deuterium data points (as seen in figure 2). Both, the measured values as well as the model prediction increase together with increasing pressure. No significant isotope mass dependence is

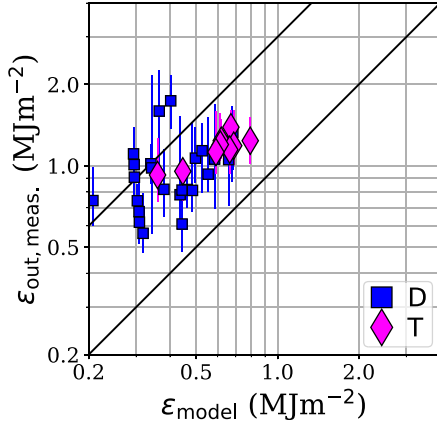


Figure 8. ELM energy fluence measured on the outer divertor target $\epsilon_{\text{out,meas.}}$ in deuterium (blue) and tritium (magenta) plasmas compared to the model prediction ϵ_{model} in a log-log plot. The 1:1 and 3:1 lines are shown in black.

visible. This is a confirmation that the model indeed captures the main transport mechanism during ELMs.

The ELM duration in this data set for both deuterium and tritium plasmas is of the order of 2.2–2.5 ms. An explicit ion mass dependence through the ion transit time ($\propto \sqrt{A}$) in the scrape-off layer is embedded in the free-streaming-particle approach [32]. The free-streaming-particle approach is able to explain the temporal evolution of single ELM filaments [33] and short ELMs at high pedestal top temperature [34, 35]. However, the ELM duration in this data set is significantly longer than the ion transit time. The longer ELM duration is observed at higher pedestal top density and lower pedestal top temperature. This is obtained in the JET-ILW baseline scenario at low heating power or when high gas fuelling is applied in order to maintain stationary conditions and avoid W accumulation [35]. The longer ELM duration is attributed to an increased lifetime of the MHD activity upstream [35, 36]. No explicit ion mass dependence has been observed under these experimental conditions.

4. Power fall-off length comparison between deuterium and tritium

A heuristic derivation of the power fall-off length by Goldston leads to the HDM [6]

$$\langle \lambda \rangle^{\text{HDM}} = \begin{cases} \frac{4a}{ZeB_{\text{pol}}R_{\text{geo}}} \left(\frac{Am_p T_{\text{sep}}}{(1+Z)} \right)^{\frac{1}{2}} & \text{ion drift} \\ \frac{4a}{eB_{\text{pol}}R_{\text{geo}}} \left(\frac{Am_p T_{\text{sep}}}{(1+Z)} \right)^{\frac{1}{2}} & \text{electron drift} \end{cases} \quad (5)$$

with e the elementary charge, T_{sep} separatrix temperature, m_p proton mass and Z and A average ion charge and mass, respectively. The conversion of poloidally averaged value to the outer MP value is done by introducing

$$\langle \lambda \rangle = \lambda \cdot \frac{B_{\text{pol,MP}} R_{\text{MP}}}{B_{\text{pol}} R_{\text{geo}}} \equiv \lambda \cdot f_{\text{geo}}^{-1}$$

with average poloidal magnetic field $B_{\text{pol}} = \frac{\mu_0 I_p}{2\pi a \sqrt{\frac{1+\kappa^2}{2}}}$. Since both deuterium and tritium have the same charge of $Z = 1$, both cases in equation (5) are equivalent and it can be simplified to

$$\langle \lambda \rangle^{\text{HDM}} = \frac{4}{\sqrt{2}} \frac{a}{R_{\text{geo}}} \frac{\sqrt{Am_p T_{\text{sep}}}}{eB_{\text{pol}}}.$$

The main uncertainty for a comparison to experimental data is the separatrix temperature T_{sep} in the model. For a negligible change in separatrix temperature between deuterium and tritium plasmas, the variation is expected to be $\lambda_q^T / \lambda_q^D = \sqrt{3/2} = 1.22$.

The most prominent scaling law for λ_q in H-mode is based on a multi-machine data set. It indicates that the poloidal magnetic field at the outer MP $B_{\text{pol,MP}}$ is the main quantity determining λ_q [5]:

$$\lambda_q^{\text{multi}}(\text{mm}) = 0.63 \cdot B_{\text{pol,MP}}^{-1.19}(T). \quad (8)$$

This scaling law is verified on most tokamaks. The exception is TCV which reports smaller values following a flux-limited approach [37]. In order to put the new JET results into context, we add the deuterium data set of Sieglin *et al* [35] from the initial JET-ILW operation. The main purpose is to provide the natural scatter of data points for a larger data set. Figure 9 shows the power fall-off length dependence on $B_{\text{pol,MP}}$ for both deuterium and tritium plasmas. Each data point represents the median value of all inter-ELM time points with reliable fit for the given time interval in which the plasma parameters are constant. The error-bars represent the 33rd and 66th percentiles as upper and lower limit. It is observed that the measurements in the tritium plasmas are close to the scaling law prediction and within the scatter of the deuterium data points. Furthermore, the measured data points display a considerable scatter around the scaling law prediction. A small variation with isotope mass, as expected by the HDM, is well within the experimental variations, especially due to the uncertainty in estimating T_{sep} experimentally.

A recent comparison of deuterium JET-CFC and JET-ILW data addressed this scatter and revealed that λ_q is anti-correlated with the pedestal top density [10]. Smaller λ_q is observed at higher pedestal density. It is noted that $n_{e,\text{ped}}$ and $B_{\text{pol,MP}}$ are strongly correlated as mentioned in section 2. Even so, the anti-correlation between $n_{e,\text{ped}}$ and λ_q is also observed for fixed $B_{\text{pol,MP}}$ in the presented data set.

It is noted that various recent studies found an anti-correlation of the volume averaged or pedestal top electron density, temperature or pressure and the power fall-off length. Notably, the H-mode multi-machine analysis found a negative exponent on the Greenwald fraction, e.g. in regressions # 10 and # 11 of [5]. Furthermore, it was shown that the power fall-off length decreases with increasing volume averaged pressure in Alcator C-Mod [7] and a similar dependence on the pedestal top pressure is reported in ASDEX Upgrade [8]. The ASDEX Upgrade study shows an anti-correlation with the pedestal density similar to the pressure. Another study

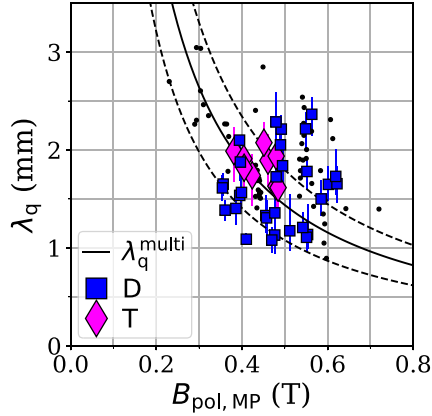


Figure 9. Power fall-off length λ_q as a function of the poloidal magnetic field at the outer MP $B_{\text{pol,MP}}$. The solid line represents $\lambda_q^{\text{multi}}(\text{mm}) = 0.63 \cdot B_{\text{pol,MP}}(T)^{-1.19}$ and the dashed lines an uncertainty interval of $\pm 25\%$ representing the scatter of the original multi-machine data set. The black dots are taken from the deuterium JET-ILW data set of Sieglin *et al* [35].

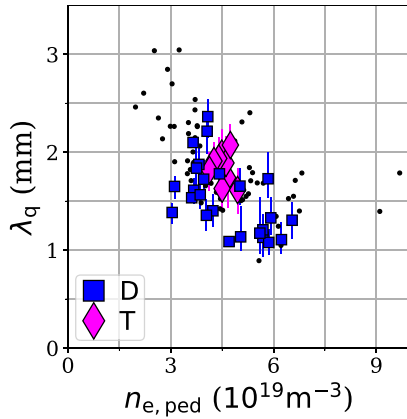


Figure 10. Power fall-off length λ_q as a function of the pedestal top density $n_{e,\text{ped}}$. The black dots are taken from the deuterium JET-ILW data set of Sieglin *et al* [35].

in ASDEX Upgrade, focusing on the the temperature fall-off length, reports on an about constant value at increasing line averaged density as long as the divertor is attached [38]. The correlation with the separatrix density, on the other hand, is different. A recent study in ASDEX Upgrade reports on a broadening of the temperature and pressure fall-off length with increasing separatrix density [39]. An increase of the power fall-off length with increasing separatrix density is also observed in the QCE regime in ASDEX Upgrade [9, 40] and in inter-ELM phases in MAST [41]. A detailed analysis of the separatrix density is outside of the scope of the here presented analysis. Extrapolating from the presented pedestal top value to the separatrix value is not possible as there is likely no strict relation between the two.

Figure 10 presents the power fall-off length as a function of $n_{e,\text{ped}}$. Similar to [10] the data set presented here exhibits less variation as function of $n_{e,\text{ped}}$ instead of $B_{\text{pol,MP}}$. Within the scatter of the data, also in the comparison with $n_{e,\text{ped}}$ no

significant difference between deuterium and tritium plasmas is observed.

From the analysis presented in this section it is concluded that available scaling law predictions based on deuterium plasmas are in agreement with the measurements in tritium plasmas and no strong isotope mass effect is visible. This is an important validation towards a D-T mixed plasma operation in next step devices like ITER.

5. Summary and conclusions

The effect of changing the plasma species from deuterium to tritium is investigated for the two main exhaust challenges of the type-I ELMy H-mode, the type-I ELM energy fluence and the narrow inter-ELM power fall-off length. For the energy fluence, the predictions from a model using energy balance considerations [15] are in line with the absence of an explicit mass dependence of the outer target energy fluence. The pedestal top pressure in tritium plasmas is slightly higher than in deuterium plasmas with similar engineering parameters, in agreement with the analysis in [26, 27]. The measured values in both, deuterium and tritium plasmas are within the 1:1 and 3:1 boundaries from the model, similar to the original experimental study in deuterium [15]. The variation in pedestal top pressure between deuterium and tritium is captured by the pressure dependence in the model. In fact, the model predictions for the in-out asymmetry is verified as well with measurements on both divertor targets in deuterium plasma pulses. The parallel energy fluence measured on the inner target is a factor of 1.08 larger than the one measured on the outer target.

For the inter-ELM power fall-off length λ_q no strong explicit ion mass dependence is observed. The measurements in deuterium as well as in tritium plasmas are within the H-mode multi-machine scaling law prediction. Similar to previous work in JET, the pedestal top density has a stronger correlation than the poloidal magnetic field, with smaller λ_q with increasing density. Theoretical and heuristic considerations that scale with the gyro-radius, e.g. the heuristic drift-based model by Goldston [6], predict a weak explicit ion mass dependence. The gyro-radius broadens with the square-root of the ion mass. However, due to the uncertain separatrix temperature, the predicted effect is well within the measurement uncertainties.

Acknowledgments

The authors would like to thank B. Sieglin for providing the JET λ_q data base for the initial JET-ILW operation. This work has been carried out within the framework of the EUROfusion Consortium, funded by the European Union via the Euratom Research and Training Programme (Grant Agreement No. 101052200—EUROfusion). Views and opinions expressed are however those of the author(s) only and do not necessarily reflect those of the European Union or the European Commission. Neither the European Union nor the European Commission can be held responsible for them.

Appendix. Heat flux analysis with infrared thermography

The divertor heat flux is calculated using the THEODOR code [42, 43] with the surface temperature from the infrared thermography [44, 45] measurements as input.

To be compatible with the high neutron rate in the D-T phase, one IR camera system—used here for the outer divertor target view—was moved outside the torus hall. The details of the viewing geometry is presented in [46]. In order to observe the outer strike line location with the IR camera system, a toroidal extension of tile 6 was installed, allowing the observation through a tile gap of the vertical outer target. The tile extension is manufactured from carbon with a tungsten coating. However, the coating has developed significant deterioration during the here analysed measurement campaigns. Poloidally localised regions with increased thermal response—so called hot spots—are visible. Two measures are taken to mitigate the surface change in the heat flux evaluation for $JPN > 92\,505$.

First, a constant heat transmission coefficient α is introduced in THEODOR. This value mimics surface layers with reduced heat capacity and thermal contact, commonly used for carbon PFCs. The numerical value $\alpha = 1.0 \frac{\text{MW}}{\text{m}^2\text{K}}$ is selected. This is the largest value with which negative integrated power load estimates after the ELMs are mitigated. The heat transmission coefficient acts like a low pass filter. The corresponding time constant τ_α is in the order of $\tau_\alpha = O(10^{-5}\text{ s})$ for the chosen numerical value following the estimation of [28]. This is smaller than the frame rate and, thus, not limiting the analysis.

Second, a zone on the outer divertor target from $R = 2.915\text{ m}$ to $R = 2.935\text{ m}$ (with the s -coordinate $1478\text{ mm} < s < 1500\text{ mm}$) exhibits a high amount of hot spots. This part of the tile is excluded for further analysis after the heat flux calculation. The strike line location in the experiment was chosen such that the peak heat flux location for both ELMs and inter-ELM is outside of this region.

In addition to this measures, the line profiles for both inner and outer target are extracted from a rectangular window within the camera frame. Within this, the toroidal minimum is used for the extraction of the photon flux along the target coordinate. This ensures that very localised hot spots are filtered out.

The inter-ELM analysis is performed using the FEET code [47]. This code takes as input the time evolution of the heat flux as well as information about the pulse behaviour. It separates inter- and intra-ELM time points. Each inter-ELM time point is fitted with the 1D diffusive model introduced by Eich et al [48]








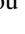
$$q(s) = \frac{q_0}{2} \exp\left(\left(\frac{S}{2\lambda_q}\right)^2 - \frac{s}{\lambda_q f_x}\right) \cdot \operatorname{erfc}\left(\frac{S}{2\lambda_q} - \frac{s}{S f_x}\right) \left(\frac{\text{MW}}{\text{m}^2}\right) \quad (\text{A.1})$$

with s target coordinate, S divertor broadening, λ_q power fall-off length and f_x flux expansion. Profile fits are only regarded reliable if they fulfil:

- $\lambda_q \cdot f_x > 2.05\text{ mm}$, which is the initial value of the fitting routine
- $\lambda_q < 3\text{ mm}$, to exclude outliers that are not within the standard deviation of the time window for the presented data set
- $\lambda_q > 1.2 \cdot S$, below which the profile is dominated by the Gaussian divertor broadening S
- $q_0 > 5\text{ MW m}^{-2}$, filtering out very low heat flux data.

All reliable time points within a steady state window are then averaged (taking the median) to extract the representative power fall-off length and error-bars (33rd and 66th percentiles).

ORCID iDs

- M. Faitsch  <https://orcid.org/0000-0002-9809-7490>
 I. Balboa  <https://orcid.org/0000-0002-5665-2222>
 S.A. Silburn  <https://orcid.org/0000-0002-3111-5113>
 A. Tookey  <https://orcid.org/0009-0009-6089-7634>
 D. Kos  <https://orcid.org/0000-0002-9550-4329>
 A. Huber  <https://orcid.org/0000-0002-3558-8129>
 E. de la Luna  <https://orcid.org/0000-0002-5420-0126>
 D. Keeling  <https://orcid.org/0000-0002-3581-7788>
 A. Kappatou  <https://orcid.org/0000-0003-3341-1909>

References

- [1] Loarte A. et al 2007 *Nucl. Fusion* **47** S203
- [2] Pitts R. et al 2013 *J. Nucl. Mater.* **438** S48
- [3] Kukushkin A., Pacher H.D., Pacher G.W., Kotov V., Pitts R.A. and Reiter D. 2013 *J. Nucl. Mater.* **438** S203
- [4] Goldston R., Reinke M.L. and Schwartz J.A. 2017 *Plasma Phys. Control. Fusion* **59** 055015
- [5] Eich T. et al 2013 *Nucl. Fusion* **53** 093031
- [6] Goldston R.J. 2012 *Nucl. Fusion* **52** 013009
- [7] Brunner D., LaBombard B., Kuang A.Q. and Terry J.L. 2018 *Nucl. Fusion* **58** 094002
- [8] Silvagni D., Eich T., Faitsch M., Happel T., Sieglin B., David P., Nille D., Gil L. and Stroth U. 2020 *Plasma Phys. Control. Fusion* **62** 045015
- [9] Faitsch M., Eich T., Harrer G.F., Wolfrum E., Brida D., David P., Griener M. and Stroth U. 2021 *Nucl. Mater. Energy* **26** 100890
- [10] Faitsch M., Eich T. and Sieglin B. 2020 *Plasma Phys. Control. Fusion* **62** 085004
- [11] Scarabosio A., Eich T., Herrmann A. and Sieglin B. 2013 *J. Nucl. Mater.* **438** S426
- [12] Sieglin B., Eich T., Faitsch M., Herrmann A. and Scarabosio A. 2016 *Plasma Phys. Control. Fusion* **58** 055015
- [13] Faitsch M., Maurizio R., Gallo A., Coda S., Eich T., Labit B., Merle A., Reimerdes H., Sieglin B. and Theiler C. 2018 *Plasma Phys. Control. Fusion* **60** 045010
- [14] Fundamenski W. et al 2011 *Nucl. Fusion* **51** 083028
- [15] Eich T., Sieglin B., Thornton A.J., Faitsch M., Kirk A., Herrmann A. and Suttrop W. 2017 *Nucl. Mater. Energy* **12** 84
- [16] Klimov N. et al 2009 *J. Nucl. Mater.* **390** 721
- [17] Loewenhoff T., Linke J., Pintsuk G., Pitts R.A. and Riccardi B. 2015 *J. Nucl. Mater.* **463** 202
- [18] Gunn J., Carpentier-Chouchana S., Dejarnac R., Escourbiac F., Hirai T., Komm M., Kukushkin A., Panayotis S. and Pitts R.A. 2017 *Nucl. Mater. Energy* **12** 75

- [19] Scarabosio A., Fuchs C., Herrmann A. and Wolfrum E. 2011 *J. Nucl. Mater.* **415** S877
- [20] Knolker M. et al 2018 *Nucl. Fusion* **58** 096023
- [21] Chang C.S. et al 2017 *Nucl. Fusion* **57** 116023
- [22] Joffrin E. et al 2017 *Nucl. Fusion* **57** 086025
- [23] Frassinetti L. et al 2021 *Nucl. Fusion* **61** 016001
- [24] Pasqualotto R., Nielsen P., Gowers C., Beurskens M., Kempenaars M., Carlstrom T. and Johnson D. 2004 *Rev. Sci. Instrum.* **75** 3891
- [25] Groebner R.J., Mahdavi M.A., Leonard A.W., Osborne T.H. and Porter G.D. 2002 *Plasma Phys. Control. Fusion* **44** A265
- [26] Frassinetti L. et al 2023 *Nucl. Fusion* **63** 112009
- [27] Schneider P. et al 2023 *Nucl. Fusion* **63** 112010
- [28] Eich T., Andrew P., Herrmann A., Fundamenski W., Loarte A. and Pitts R.A. (JET-EFDA contributors) 2007 *Plasma Phys. Control. Fusion* **49** 573
- [29] Gunn J. et al 2017 *Nucl. Fusion* **57** 046025
- [30] Pitts R. et al 2017 *Nucl. Mater. Energy* **12** 60
- [31] Krieger K. et al 2023 *Nucl. Fusion* **63** 066021
- [32] Fundamenski W. and Pitts R.A. (JET EFDA contributors) 2005 *Plasma Phys. Control. Fusion* **48** 109
- [33] Adamek J. et al 2020 *Nucl. Fusion* **60** 096014
- [34] Eich T., Kallenbach A., Fundamenski W., Herrmann A. and Naulin V. 2009 *J. Nucl. Mater.* **390–391** 760
- [35] Sieglin B. et al 2013 *Plasma Phys. Control. Fusion* **55** 124039
- [36] Pamela S. et al 2015 *Plasma Phys. Control. Fusion* **58** 014026
- [37] Maurizio R., Duval B.P., Labit B., Reimerdes H., Faitsch M., Komm M., Sheikh U. and Theiler C. (the TCV team) 2021 *Nucl. Fusion* **61** 024003
- [38] Sun H.J. et al 2017 *Plasma Phys. Control. Fusion* **59** 105010
- [39] Eich T., Manz P., Goldston R.J., Hennequin P., David P., Faitsch M., Kurzan B., Sieglin B. and Wolfrum E. 2020 *Nucl. Fusion* **60** 056016
- [40] Faitsch M. et al 2023 *Nucl. Fusion* **63** 076013
- [41] Harrison J. Fishpool G.M. and Kirk A. 2013 *J. Nucl. Mater.* **438** S375
- [42] Herrmann A., Junker W., Gunther K., Bosch S., Kaufmann M., Neuhauser J., Pautasso G., Richter T. and Schneider R. 1995 *Plasma Phys. Control. Fusion* **37** 17
- [43] Sieglin B., Faitsch M., Herrmann A., Brucker B., Eich T., Kammerloher L. and Martinov S. 2015 *Rev. Sci. Instrum.* **86** 113502
- [44] Balboa I. et al 2012 *Rev. Sci. Instrum.* **83** 10D530
- [45] Balboa I. et al 2016 *Rev. Sci. Instrum.* **87** 11D419
- [46] Balboa I. et al *Plasma Phys. Control. Fusion* **65** 094002
- [47] Burge C.D. 2019 UKAEA-CCFE-RE(23)31 *Internal Report* (UKAEA)
- [48] Eich T., Sieglin B., Scarabosio A., Fundamenski W., Goldston R.J. and Herrmann A. 2011 *Phys. Rev. Lett.* **107** 215001